RESEARCH ARTICLE

WILEY

Three-dimensional investigation of an open- and a closed-system Pingo in northwestern Canada

Julius Kunz 🅾 | Christof Kneisel 🅾

University of Wuerzburg, Institute of Geography and Geology, Wuerzburg, Germany

Correspondence
Julius Kunz, Institute of Geography and Geology, University of Wuerzburg, Am Hubland, 97074 Wuerzburg, Germany.
Email: julius.kunz@uni-wuerzburg.de

Funding information
German Research Foundation (DFG), Grant/Award Number: KN542/15-1

Abstract

The present study presents three-dimensional investigations of a hydrostatic pingo in the Mackenzie Delta region and a hydraulic pingo in the Ogilvie Mountains and contributes to a better understanding about the internal structures of the two pingo types. A combined approach using quasi-three-dimensional electrical resistivity tomography, ground-penetrating radar and frost probing allowed a clear delineation of frozen and unfrozen areas in the subsurface. At the hydrostatic pingo a massive ice core as well as a surrounding talik could be detected, but the location of the ice core and the talik differs from previous published assumptions. In contrast to acknowledged theory, at our site the massive ice core is not located in the center of the pingo but at the western edge, whereas the eastern flank is underlain by a talik, which surrounds the massive ice core. At the hydraulic pingo, the expected internal structure could be confirmed and the pathway of upwelling water could also be detected. The combined approach of the applied methods represents the first known three-dimensional geoelectrical investigation of pingos and provides new insights into the internal structure and architecture of the two different pingo types. The chosen approach allows further conclusions on the formation of these permafrost-affected landforms.

KEYWORDS
near surface multidimensional geophysics, permafrost, permafrost hydrology, pingos

1 | INTRODUCTION

Pingos are perennial, conical, ice-cored hills with a diameter of several decameters or hundreds of meters and a base height between a few meters and several decameters.[1,2] The first description of a pingo in northern Canada was by Richardson.[3] Leffingwell[4] had previously supposed hydraulic pressure as a reason for the formation of these features. Porsild[5] developed a second model of pingo genesis based on formation in a closed hydrological system. These two studies represent the basis of the theories of hydrostatic- and hydraulic-system pingo genesis, which are still recognized today.

The origin of pingos has been studied for several decades, and in the Mackenzie Delta region hydrostatic pingos have been investigated intensively by J. R. Mackay. In contrast, the formation of hydraulic pingos is far less investigated. Due to different possibilities of artesian water pathways and origins, there are still uncertainties regarding hydraulic pingo formation.

Mackay[6] started to investigate the hydrostatic (closed-system) pingos in the Mackenzie Delta region and developed a conceptual model of hydrostatic pingo formation based on numerous studies in the region. He investigated the relationship between drained lakes and the refreezing of taliks and unfrozen sediments, respectively.

According to this, in particular the drainage of former lakes and the subsequent downward and upward growth of permafrost in the area of the former sublake talik is evident for the formation of a closed system and hydrostatic pressure (e.g.,[2,7]). Based on drillings he was able to show the presence of intrusive and segregation ice and even verified the hydrostatic pressure in a closed water lens below the uplifted pingo.[2,8] Mackay also explored the growth rates of hydrostatic pingos in the Mackenzie Delta region and determined different growth rates during different stages of pingo genesis. While growth rates could reach more than 1 m during the first years of pingo genesis, the growth rates decrease with advancing age of the pingo to several centimeters per year.[9,10]

The open-system type (hydraulic pingo) was further investigated by Müller,[11] who discussed the role of intra- and subpermafrost water and the ascent of water under artesian pressure in East Greenland. O'Brien[12] posited a direct link between hydraulic pingos and rock fractures, which probably act as water pathways. One of the most common theories of hydraulic pingo formation is that of Liestøl,[13] who assumed a connection between pingo formation and subglacial meltwater drainage beneath polythermal glaciers within the catchment area in Svalbard. He later investigated the water discharge of pingo springs and their physical processes and mechanisms.[14] In addition to hydraulic pingos associated with geological faults or subglacial melt-/groundwater, Yoshikawa and Harada[15] introduced a third type of hydraulic pingos. These are related to geological uplift of the land surface or a relative sea level drop and are located in nearshore areas. Humlum et al.[16] discussed the role of coarse-grained materials in alluvial fans, which lead to water flow within the fan and a relative uplift of the water at the lowermost end of the fan, where the sediments become thinner. In a recent study, transitional forms between hydrostatic and hydraulic pingos have been investigated, which developed in phases in both open and closed systems.[17] Figure 1 schematically illustrates and summarizes the main differences in the formation of hydrostatic and hydraulic pingos based on the aforementioned literature.

Most of these studies are based on observations at the surface, drillings, or natural outcrops. Restrictions related to these observations are the lack of two- or three-dimensional (2D, 3D) information or destroyed systems in the case of eroded outcrops. Geophysical

investigations of pingos are quite rare,[18–22] but the few studies could provide interesting 2D information about the internal structures of intact and undestroyed pingos.

In the context of global warming, the processes of water movement and hydrogeological subsurface conditions as well as the still fairly unknown permafrost hydrology are becoming more important and their investigation is therefore of great interest.[23–25] Hence, the aim of this study is the 3D geophysical investigation of the two pingo types, a hydraulic pingo and a hydrostatic pingo. The 3D approach allows a detailed investigation of the subsurface architecture. This contributes to a better understanding of water pathways in the subsurface and allows further conclusions on the formation of these permafrost-affected landforms.

2 | STUDY SITES

Both investigated pingos are located in northwestern Canada. While the hydrostatic pingo east of the Mackenzie Delta (Northwest Territories) is located in an area of continuous permafrost, the hydraulic pingo is situated in the Ogilvie Mountains (Yukon Territories), lying in the transition zone between continuous and discontinuous permafrost.[26]

2.1 | Hydrostatic pingo

The investigated hydrostatic pingo (Figure 2) is located in the transition zone of the Cariboo Hills and the southern part of the Tuktoyaktuk Peninsula near Parsons Lake close to the Inuvik–Tuktoyaktuk Highway. The region is underlain by continuous permafrost, which is 300–400 m thick and characterized by permafrost temperatures between −5 and −6°C.[29,30] The upper few meters or decameters of the permafrost are partly ice-rich, which is due to the high content of pore ice in sandy sediments and the formation of large amounts of segregation ice because of high pore-water pressures during the deglaciation of the region. At some places in the region, the existence of basal ice of the former Laurentide Ice Sheet was also proven.[29,31] The climate of the region is characterized by
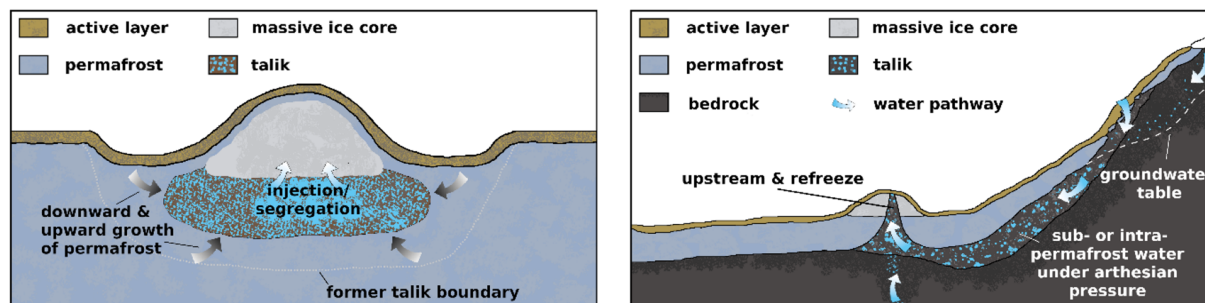
FIGURE 1 Schematic illustration of hydrostatic (left) and hydraulic (right) pingo formation [Colour figure can be viewed at wileyonlinelibrary.com]
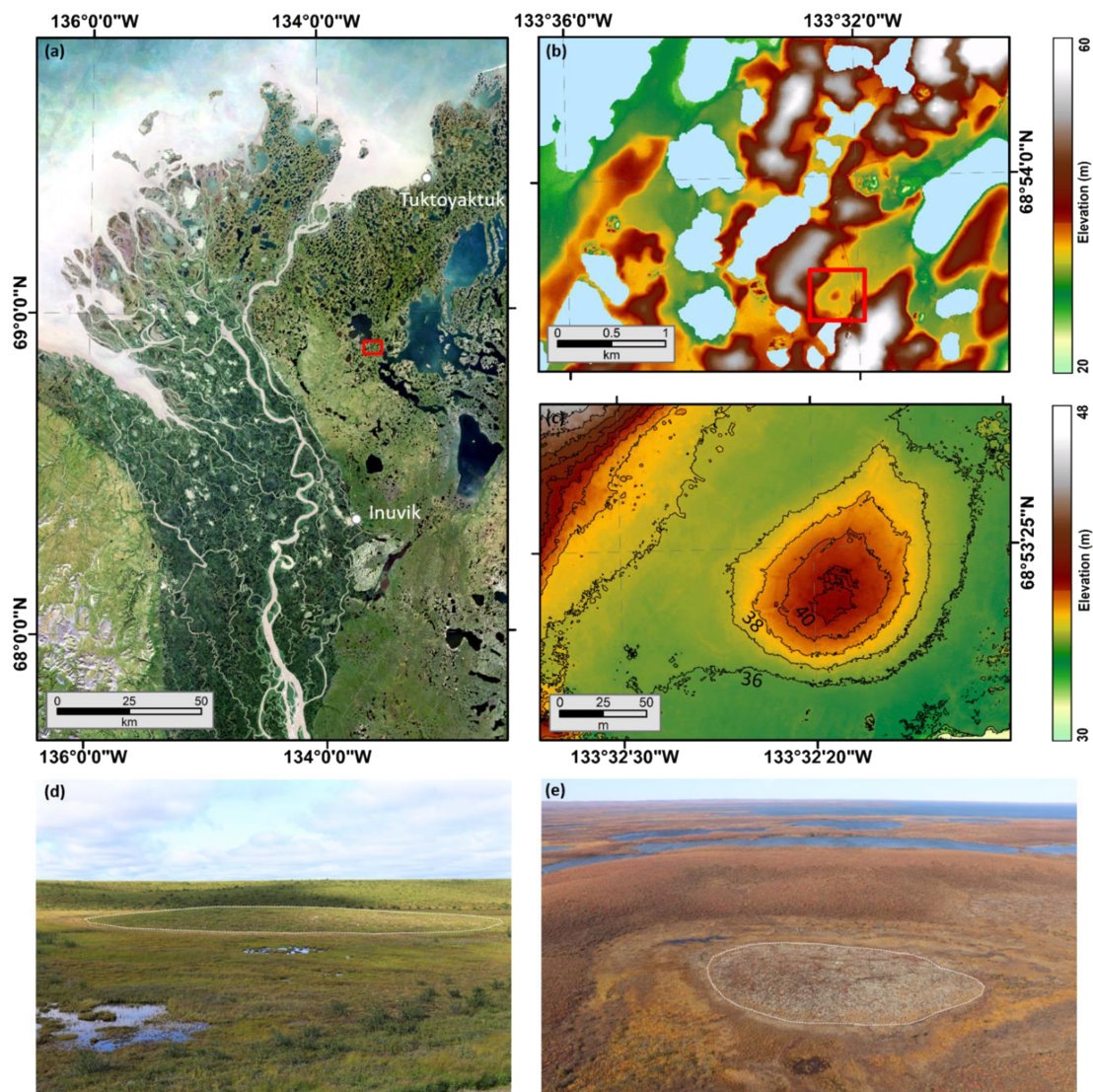
FIGURE 2 Hydrostatic pingo site. (a) Landsat-8 RGB true-color image composite (July and August; 2015–2018) of the Mackenzie Delta region generated according to the approach of Nill et al.[27] (b) Arctic DEM[28] of the study area southeast of Parsons Lake. (c) High-resolution photogrammetric DEM of the pingo derived from in situ UAV acquisitions. Elevation contours have an interval of 1 m. Location of the study site is marked with a red box in (a) and (b). (d) Ground-based photograph of the pingo in August 2018 (photo in northwestern direction). (e) Aerial photograph of the pingo in September 2019 (photo in northwestern direction). The boundary of the elevated pingo is marked by a dashed line in (d) and (e) [Colour figure can be viewed at wileyonlinelibrary.com]

mean annual air temperatures between −10.1°C (Tuktoyaktuk) and −8.2°C (Inuvik) (climate normal 1981–2010).[32,33] During the same period, precipitation was between 160 mm (Tuktoyaktuk)[32] and 241 mm (Inuvik).[33] These values are quite low due to the long sea ice season in the Beaufort Sea and the related low evaporation rates. The study site is located north of the tree line and the vegetation is mainly characterized by dwarf shrubs, tussocks, herbs, and lichens. In depressions, typical vegetation of sedge tundra and along small creeks riparian shrubs also dominate the vegetation. The zonation of different vegetation forms related to different relief positions is evident in this area, similar to that determined by Grünberg et al.[34]

The morphology of this region is characterized by a hilly relief between 20 and 60 m a.s.l. and a large number of small- or mesoscale periglacial landforms such as pingos, ice wedge polygons and

hummocks. A large number of thermokarst lakes dominate the terrain. They undergo major dynamics such as thaw subsidence or thermal erosion and retrogressive thaw slumping in the littoral zones. The dynamics of such lake landscapes in ice-rich permafrost regions have led in the past and currently to rapid drainage or silting up of lakes. The investigated pingo is situated in one of those drained lakes. The pingo is characterized by a slightly elongated/oval shape and is 190 m long and 140 m wide. With a base height of ∼4.5 m above the surrounding former lake floor it is not particularly high, but it is clearly uplifted from the surrounding former lake bottom. The surface of the pingo is characterized by numerous prominent frost cracks (cf. Figure 2c). Due to its low base height and relatively large diameter, the pingo is classified as broad-based according to the differentiation of Walker et al.[35] Therefore the pingo differs from most of the other

pingos in the Tuktoyaktuk Peninsula area, which are mostly classified as steep-sided.[2,8]

2.2 | Hydraulic pingo

The hydraulic pingo site (Figure 3) is located in the transition zone of discontinuous and continuous permafrost in the Ogilvie Mountains, which reach altitudes of up to 2,300 m a.s.l. in the area of Tombstone Territorial Park. The climate station in Dawson City (95 km to the south) is used as a reference due to the lack of climate data in the region. The station is characterized by mean annual air temperatures of −4.1°C and annual precipitation of 324 mm (climate normal 1981–2010).[36] Annual precipitation at the investigated pingo site should be slightly higher, because of the higher elevation of the Ogilvie Mountains, but temperature should be quite similar due to atmospheric inversion settings during the winter months.[37,38] In several studies along the Dempster Highway permafrost temperatures between −2.7 and −3.7°C were measured between North Fork Pass and Chapman Lake within the eastern Blackstone River Valley.[39,40] The relatively broad valleys of the eastern and western Blackstone River are filled with glacial till, whose chronological origin remains under discussion. The age of the Chapman Lake terminal moraine was dated in several studies to the Middle Pleistocene Reid glaciation[38] as well as to the younger, Late Pleistocene McConnell glaciation.[41] The more common theory, however, is that the moraine was formed
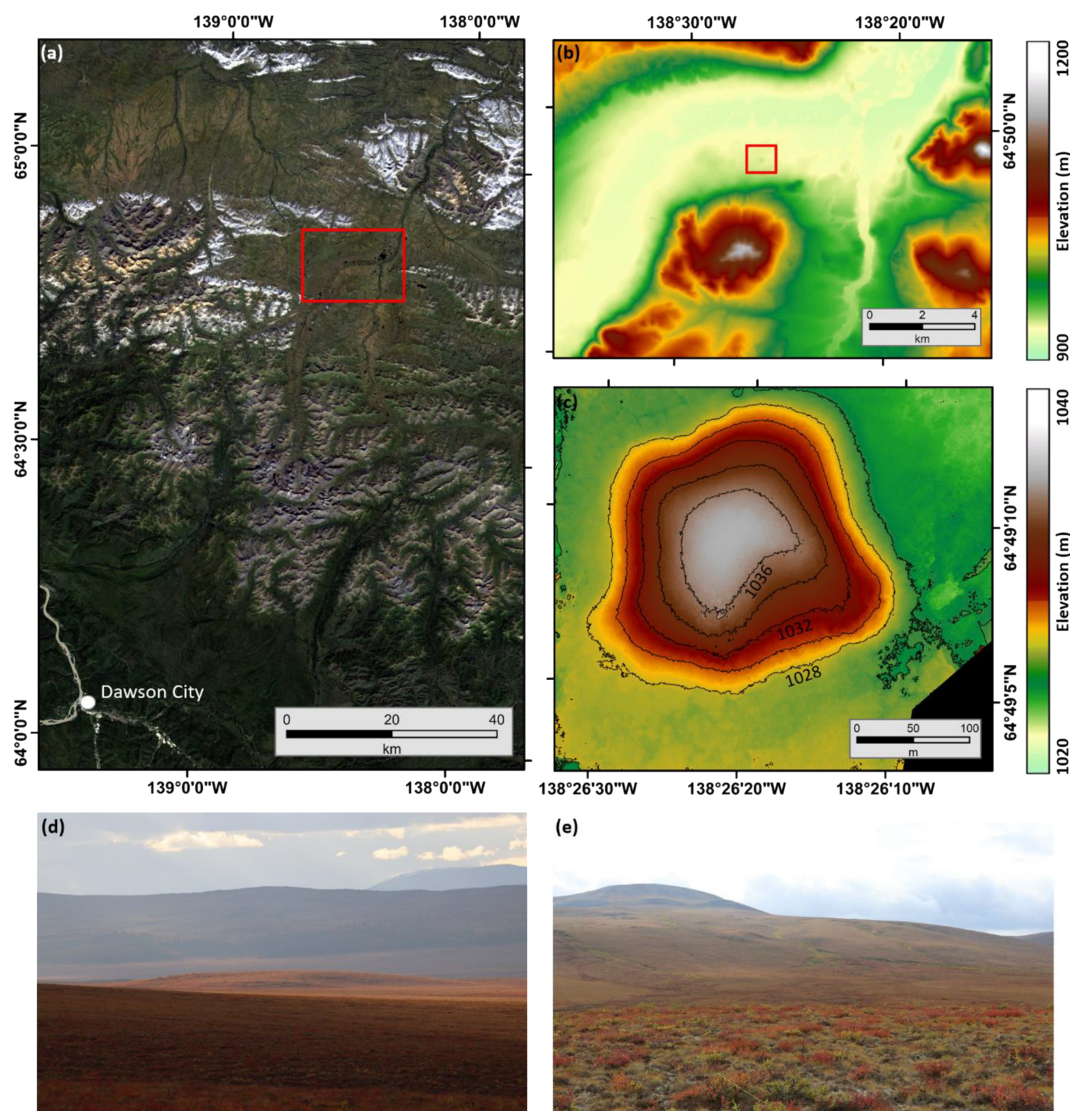
FIGURE 3 Hydraulic pingo site. (a) Landsat-7 & -8 RGB true-color image composite (July and August; 2014–2019) of the Tombstone Territorial Park area in the Ogilvie Mountains generated according to the approach of Nill et al.[27] (b) Arctic DEM[28] of the study area southwest of Chapman Lake. (c) High-resolution photogrammetric DEM of the pingo derived from in situ UAV acquisitions. Elevation contours have an interval of 2 m. Location of the study site is marked with a red box in (a) and (b). (d) Ground-based photograph of the pingo in August 2019 (photo in western direction). (e) Photograph of the south-bordering hillslope with incised streams and vegetation-covered alluvial fans from top of the pingo [Colour figure can be viewed at wileyonlinelibrary.com]

during the Reid Glaciation. The pingo is situated in the western Blackstone River Valley 5 km southwest of Chapman Lake at the foot of a north-facing hillslope at ~1,020 m a.s.l. The location is also within the Chapman Lake terminal moraine stage and characterized by glacial till as well as fluvial and alluvial sediments. The diameter of the pingo is ~280 m and the base height is about 12 m. Well-developed polygonal structures and some small streams from the south-bounding hillslope surround the pingo. In contrast to the other investigated pingo, no large cracks are visible at the surface of the pingo.

During some drillings near Chapman Lake, Idrees et al.[39] were able to confirm the existence of a talik or unfrozen area under an ~7-m-thick layer of ice-rich permafrost, indicating groundwater flow towards the unfrozen Blackstone Riverbed. In addition, large icing events during the winter months near and within the riverbed of the Blackstone River indicate the existence of groundwater flow within or beneath the permafrost layer.[39,42] A few kilometers southeast of the pingo, Lacelle et al.[38] confirmed the presence of massive ground ice of glacial origin, indicating different types and possibly various ages of ground ice in this region.

3 | METHODS

A multimethodological approach was used to study the internal structures of the two pingos. The main focus was on a geophysical characterization of the pingo subsurface using electrical resistivity tomography (ERT) and ground-penetrating radar (GPR). These methods were promoted by Yoshikawa et al.[19] as being the most appropriate geophysical methods for the investigation of pingos. In addition, frost probing was performed to measure the active layer thickness (ALT). A terrain analysis based on high-resolution photogrammetric digital elevation models (DEM) generated from unmanned aerial vehicle (UAV)-based images complemented the approach. Only a brief introduction into the basic approaches is given because most of the methods are commonly used in the field of periglacial landform investigation.[43,44]

3.1 | Frost probing

For the frost probing, a 120-cm-long steel rod was pushed into the ground to detect the depth of the frost table and ALT. The measured depths roughly match the depth of the permafrost table, as the measurements were performed at the end of the melt season in late August and/or early September. All measurements were rounded to an accuracy of 5 cm, as the surface could not be determined to centimeter precision due to the vegetation cover.

3.2 | Quasi-3D ERT

Geoelectrical methods such as ERT use the variability of the electrical conductivity of different materials (e.g., sediments, air, water, or ice)

to investigate the spatial distribution of different materials within the subsurface.[45] For this two current electrodes are used to inject a direct current into the subsurface, while two additional potential electrodes measure the potential field within the subsurface. The apparent electrical resistivity of the subsurface could be determined using Ohm's law and an electrode arrangement-dependent correction factor. The arrangement of these four electrodes is given by the chosen electrode array, which affects the spatial resolution and penetration depth.[45,46] However, the method of 2D or 3D ERT not only uses four electrodes, but a large number of electrodes, which are arranged in a straight line or in a 3D grid and connected to a corresponding multicore cable. This enables an automatic switching between all possible electrode configurations of the chosen electrode array along the line or within the grid. Thus, the measurement of a large number of individual data points is possible in a comparatively short time. The so-called quasi-3D approach describes the measurement of several parallel or orthogonal 2D profiles whose point data are merged and inverted three-dimensionally.[47] The resulting pseudosections provide insights into the distribution of the apparent electrical resistivity within the subsurface. This method enables a delineation of frozen and unfrozen materials and can deliver information regarding the ice content in the subsurface, as materials such as ice and water are characterized by different resistivity values. As the permanently frozen area is usually characterized by a mixture of ice, mineral substrate, and also a proportion of liquid pore water, the resistivity can vary considerably. In particular, variations in the water content or ice saturation can complicate a clear delineation of frozen and unfrozen material.

In this study, we used a Syscal Pro Switch 72 from IRIS Instruments Inc. (Orléans, CN, France) and measured Wenner-Schlumberger and Dipole–Dipole arrays with 72 electrodes in each profile. For the quasi-3D approach, we used an electrode spacing of 3 m for the longitudinal profiles (X) at both study sites. At the hydrostatic pingo site, we made additional cross profiles (Y) with an electrode spacing of 2 m. The interline spacing was 6 m (X-lines) and 12 m (Y-lines) at the hydrostatic pingo and 9 m at the hydraulic pingo. For comparison of the grids, the specifications are listed in Table 1.

TABLE 1 Specifications of the two measured quasi-3D ERT grids

	Hydrostatic Pingo	Hydraulic pingo
Number of grid lines	34 (21 X, 13 Y)	16 (X)
Electrode spacing	2 m (Y) and 3 m (X)	3 m
Interline spacing	6 m (X) and 12 m (Y)	9 m
Array type	Dipole–Dipole	Wenner-Schlumberger
Data points per profile	1,321 (X) and 1,615 (Y)	716
Number of used data points	48,322 (of 48,736)	11,451 (of 11,456)
Absolute error (iteration)	4.73% (5)	4.41% (4)

For data processing the software packages RES2DINVx64 (ver. 4.05.41) and RES3DINVx64 (ver. 3.11.73) (Geotomo Software, Gelugor, PNG, Malaysia) were used. To eliminate poor datum points a filtering with a 5% threshold of the standard deviation of the different stacks of each datum point was performed. Any point with a standard deviation more than 5% was deleted and not included in the inversion. The single profiles were inverted individually for further quality checking and poor datum points with a root-mean-square error (RMSE) of more than 100% were deleted after a trial inversion as recommended by Loke.[47] All 2D profiles were then collated into a 3D dataset and the topography was added. The electrode positions (marked after replacing of the electrodes) and the topography were derived from UAV-based orthoimage and DEMs. Inversion of the 3D dataset was performed using a robust inversion (L1 Norm) with an initial damping factor of 0.1 and a vertical to horizontal flatness filter ratio of 1.

3.3 | Ground-penetrating radar

The method of GPR uses electromagnetic waves transmitted into the subsurface by an antenna to detect structural boundaries. The signal spreads radially in the subsurface and is reflected by boundaries between materials with different dielectric characteristics. A second antenna receives the reflected signal that is saved as a function of run time, phase, and amplitude. The method enables a 2D or 3D localization of different boundaries within the subsurface, if the antennas were pulled along a profile in a fixed geometry.[45,48] In the context of permafrost research, this method is quite common because of the large contrasts in dielectric characteristics of the dominant materials. Similar to the resistivity values, the dielectric characteristics— especially the permittivity—of water and ice are also quite different.

Therefore, boundaries between these materials lead to high-amplitude reflections, which enable their detection using GPR.[49] In this study the depth of the permafrost table and its topography are of particular interest. This interface is easily detectable by GPR due to high water content in the active layer and high ice contents within the upper few meters of the permafrost and the resulting dielectric contrasts.

We used a NOGGIN system (Sensors & Software Inc., Mississauga, ON, Canada) with shielded 250-MHz antennas to detect the permafrost table at the hydrostatic pingo site. Subsequent processing of the data was carried out using the EKKO-Project-V5 Software (Sensors & Software). A background-removal filter based on the average of all profile traces, dewow filter, and topographic migration were used to optimize data quality. A spherical and exponential compensation (SEC gain) with automatic settings was then used to amplify the signal intensity and to maintain the reflection intensity of the individual reflectors. To determine the frost table topography, its reflector was picked manually along all profiles and the signal propagation velocity was calculated by comparison with manual frost probing data. The calculated and used electromagnetic wave velocity for the active layer was 0.057 m/ns.

4 | RESULTS AND INTERPRETATION

4.1 | Hydrostatic pingo

The results of frost probing (Figure 4) show a clear zonation of the active layer depth in the area of the hydrostatic pingo. While an ALT of 40 cm or less dominates in the uplifted area of the pingo, the surrounding belt is predominantly characterized by ALTs of more than 50 cm. In some sectors of the surrounding area it even reaches more
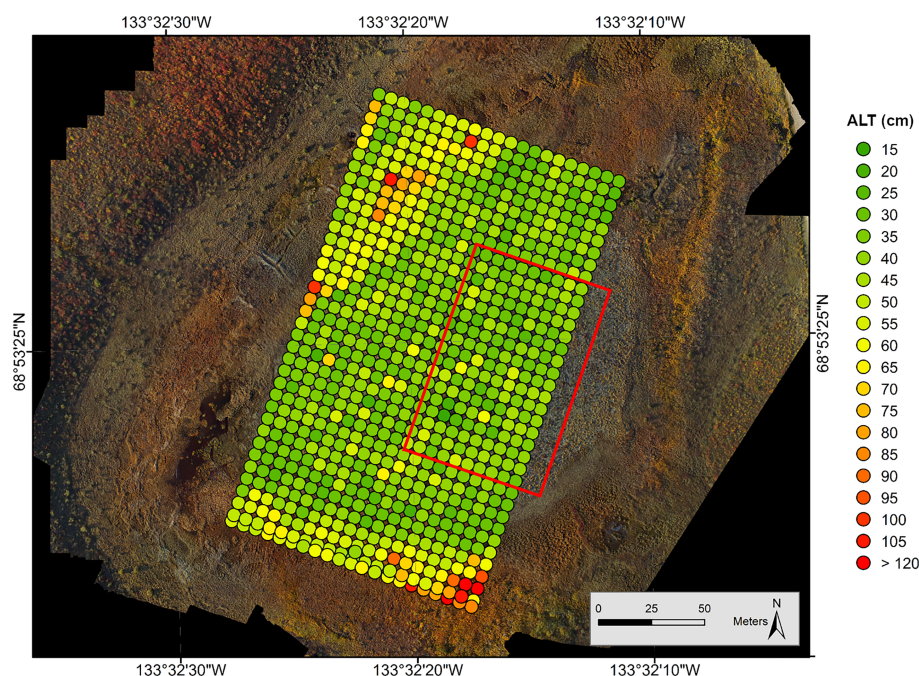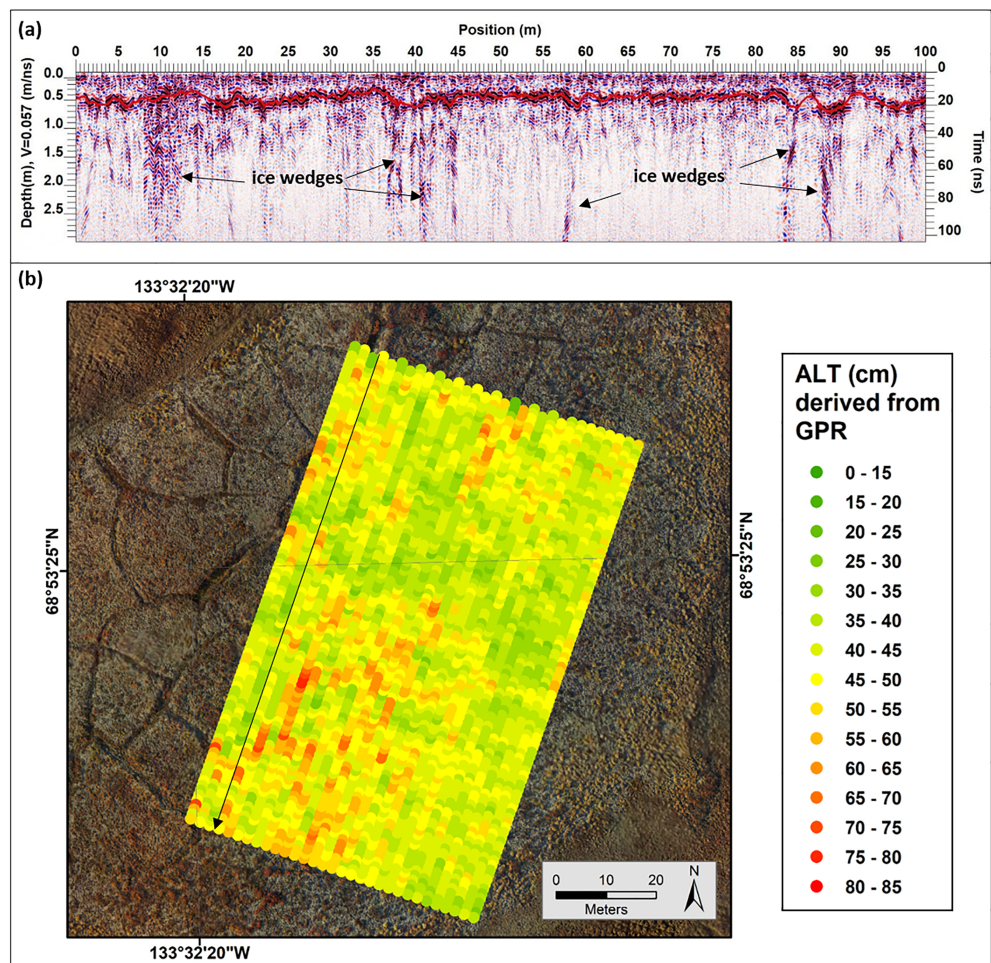

FIGURE 4 Active layer thickness (ALT, cm) determined by frost probing. The extent of the GPR grid (Figure 5) is marked by the red box. The sampling interval used was set at 6 m (at each second electrode of the quasi-3D grid) [Colour figure can be viewed at wileyonlinelibrary.com]

than 100 cm. At the southernmost edge of the grid the permafrost table could not be detected using the frost probe and the active layer must be thicker than 120 cm. A belt a few meters wide is particularly noticeable in the transition zone between the elevated pingo and its flat surroundings. This belt is characterized by an ALT less than 25 cm. In addition to the zonation, there was a notable coincidence of the ALT with the dominant type of vegetation and especially the local soil moisture. All areas outside of the elevated pingo with an ALT of more than 50 cm are dominated by sedges and are characterized by high soil moisture or even ponding water. The belt of extremely low ALTs in the transition zone is dominated by tussocks and shows lower soil moisture levels. The elevated part of the pingo is characterized by relatively dry conditions, with the exception of the sinks of frost cracks. The vegetation in this area is dominated by a mixture of dwarf shrubs, tussocks, herbs, and lichens. The sinks of the frost cracks are mostly covered by lichens and moss. Even in the central area of the pingo there are some locations with an ALT of more than 40 cm, but they do not show a consistent pattern. This is probably due to the comparatively large probe spacing of 6 m.
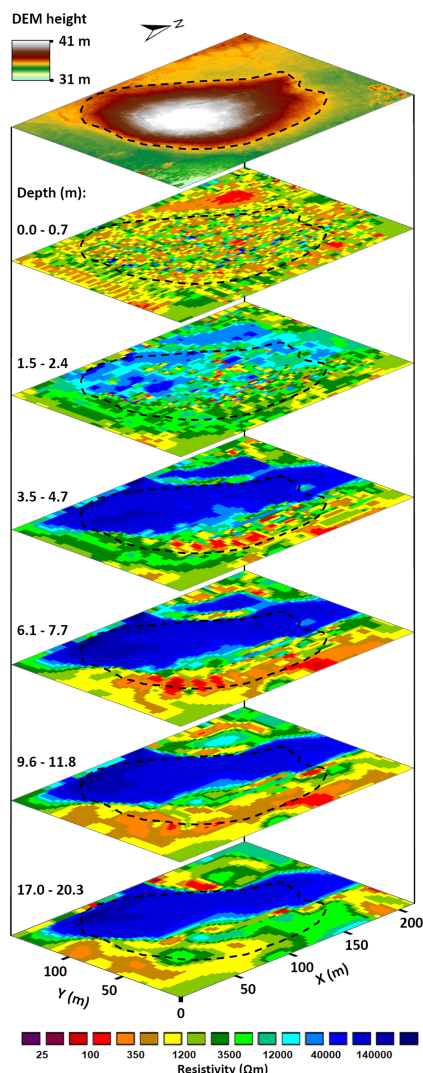
A comparison with the high-resolution UAV-based orthophoto as well as the high-resolution GPR data shows a direct link between these greater ALTs and the location of the polygonal crack structures at the surface of the pingo. The GPR measurements clearly reveal the polygonal structures and are mainly characterized by a larger depth of the permafrost table. Therefore, a map of the ALTs derived from the GPR measurements illustrates the location of the frost cracks and confirms the relationship between the ALT and these cracks (Figure 5). Additional monitoring of the ground surface temperature in one of the cracks near the center and on the plateau of an adjacent polygon (distance between the two loggers is ∼ 1 m) could also detect thermal differences between the frost crack and the surrounding undestroyed area (data not shown).

These polygonal structures are also visible in the uppermost depth slice of the 3D ERT data (Figure 6), where they appear as a mesh of cells with high resistivity values within an otherwise conductive surrounding area. This may suggest higher ice contents below the surface depressions of the cracks, despite the occurrence of larger ALTs at these locations. Otherwise, there is a heterogeneous resistivity distribution in the uppermost layer, interrupted only by a very low resistivity anomaly in the northwestern part of the grid. This can be explained by larger depressions of the permafrost table and the presence of large water-filled holes in this area. Given the low ALTs especially in the elevated area of the pingo (< 40 cm) and the depth of the first data points of the measurement (∼ 70 cm) it is assumed that

FIGURE 5 GPR-based active layer thickness measurement. (a) Example of the two-dimensional GPR profiles. The continuous reflector of the permafrost table is highlighted by a red line. (b) Active layer thickness (ALT, cm) derived from the GPR measurements are shown using a point spacing of 1 m along the GPR profiles. The black arrow marks the position and the direction of the profile shown in (a) [Colour figure can be viewed at wileyonlinelibrary.com]
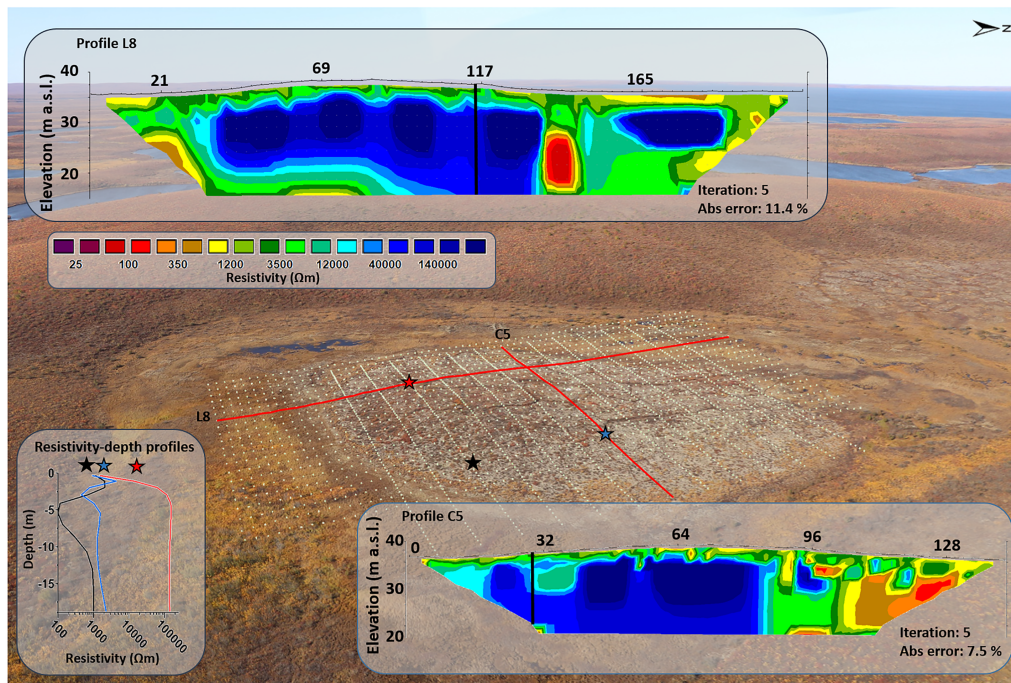
FIGURE 6 Quasi-3D ERT results and UAV-based DEM of the hydrostatic pingo. Presented are selected depth slices of the quasi-3D ERT grid dataset, which is characterized by an absolute error of 4.73% using the 5th iteration [Colour figure can be viewed at wileyonlinelibrary.com]

western part continues downwards to the lowermost layer of the model (17–20.3 m) the resistivity values in the low-resistivity anomaly decrease to a depth of 7.5 m. With increasing depth, the resistivity values remain constant or just increase slightly. Due to resistivity values lower than 800 to 1,000 Ωm, it must be assumed that this low-resistivity anomaly represents an (at least partly) unfrozen area surrounding the pingo on the eastern side. It is only at a depth of 17 m that a more pronounced increase of the resistivity values to more than 1,200 Ωm is detectable almost across the entire area of the eastern flank of the pingo. The increasing resistivity values in the lowermost model layer may represent the lower boundary of the partly unfrozen area, but this can only be interpreted with caution due to the low data density and the low model sensitivity at this depth calculated by RES3DINV. Because of the superimposed (permanently) frozen layer up to 3 m thick and the great depth up to 20 m, it must be assumed that the unfrozen layer is not part of the active layer, but rather the remnant of a talik that has underlain the former lake. The adjacent high-resistivity anomaly (> 40 kΩm) is interpreted as the massive ice core of the pingo. The shape of this massive ice core, which is about 200 m long but less than 100 m wide, is characterized by a distinct curvature. The location of the massive ice core in relation to the morphologically elevated part of the pingo is also conspicuous. Contrary to expectations, it is not located beneath the central part of the elevated surface, but rather in the northern and western flank of the pingo. At a depth between 3.5 and 11.8 m of the geophysical model, almost the entire eastern part of the elevated pingo is underlain by the low-resistivity anomaly (< 800 Ωm), which is interpreted as a talik or at least an area of partly unfrozen sediments with high amounts of liquid water. At a depth between 11.8 and 17 m, the resistivity values do not exceed 1,200 Ωm, so that permafrost cannot be unequivocally proven in this area. This asymmetric location of the massive ice core is also visible in the 2D profiles in Figure 7. In particular in profile C5 the low resistivity values below the eastern flank of the pingo are conspicuous. This asymmetry is not visible in the longitudinal direction of profile L8 because the profile is located in the western part of the pingo and the extent of the high-resistivity anomaly of the massive ice core fits exactly with the morphological shape of the pingo in this area. In the transition zone between the pingo and its surroundings (around profile meter 140) a low-resistivity anomaly is visible at a depth of more than 7 m. From profile meter 160 onwards, another high-resistivity anomaly is visible beneath a slightly thicker low-resistivity uppermost layer. This area is located beneath the higher ALTs and the ponding water at the surface in the northern part of the grid.

At the southernmost edge of the grid, where an ALT greater than 120 cm was present, the grid data show that the electrical resistivity values are also quite low. This area marks the only part of the grid where low-resistivity values continue from the surface to the underlying talik without an interruptive layer of higher resistivity values indicating a permafrost layer. This leads to the assumption that there must be a (seasonal) connection between the talik and the active layer close to the surface, so that the talik is not a (perennial) closed system. However, this does not necessarily have to be the case in every year, but can also occur only in individual years due to fluctuating ALTs.

some of the data points of the first layer represent (permanently) frozen conditions. The relatively low electrical resistivity values (< 1,200 Ωm) within this layer suggest that a high content of unfrozen water must also be present in the uppermost part of the permafrost body. With increasing depth up to 3 m, an increase of the electrical resistivity values can be detected across the whole area. Between 3 and 3.5 m depth an intense increase of the resistivity values up to more than 40 kΩm could be detected in the central, northern, and western part of the grid. In the eastern and southern part of the grid an inverse trend is visible within the model. This is shown in more detail in Figure 7 through a comparison of a longitudinal and a cross-profile and by a comparison of the resistivity depth profiles of three different positions in the grid. The eastern part is characterized by a strong decrease of resistivity values in a depth of more than 3 m. While the high-resistivity anomaly in the central, northern, and

FIGURE 7 2D ERT profiles of the 3D grid in longitudinal (L) and cross (C) direction. The labels in the photograph mark the start position of each profile. The cross point location of the two profiles is indicated with a vertical black line within the 2D profiles. The three stars mark the positions of the resistivity–depth profiles at the western (red) and eastern (black and blue) sites of the pingo, which are derived from the 3D ERT model [Colour figure can be viewed at wileyonlinelibrary.com]

4.2 | Hydraulic pingo

The ALT measurements at the location of the hydraulic pingo in the Ogilvie Mountains present a more heterogeneous pattern of ALT distribution without a distinct zonation (Figure 8). The ALT shows a small-scale variability and ranges between 20 and 95 cm. The only cluster of very low ALTs is visible at the southern foot of the pingo, were ALTs about 30 cm dominate. In the area of the two extended profiles in the southern catchment area, the results also show comparatively low ALTs. Only the crossed streams constitute an exception and are characterized by ALTs larger than 70 cm. In contrast to the other pingo, no prominent frost cracks are visible at the surface here. Hence, no correspondence between the ALT and the microrelief is recognizable.

In contrast, the results of the quasi-3D ERT grid (Figure 9) show a slight zonation of the resistivity values in the uppermost layer. In particular, in the western and southwestern part of the grid a concentration of low-resistivity values lower than 1,200 Ωm is visible. This can be due to larger ALTs and possibly higher water contents in the upper few centimeters of the permafrost body. In the other part of the grid, the uppermost layer is heterogeneous, but the resistivity values are greater than 1,200 Ωm almost everywhere. These areas may be less moist and characterized by a slightly shallower frost table. The second depth layer ($\sim$ 1.5–3.2 m depth) shows an increase of the electrical resistivity values across the entire grid to values between 3 and 20 kΩm. Only at some small single spots the electrical resistivity values remain at a low level between 350 and 1,200 Ωm. The more or

less area-wide increase of the resistivity values indicates decreasing water contents within the permafrost body and may also point to lower permafrost temperatures. The contrast between the high-resistivity layer and the low-resistivity anomaly becomes stronger with increasing depth: at a depth of 3.5 m a larger high-resistivity anomaly (> 20 kΩm) covering the southeastern quarter of the grid area appears. This high-resistivity sector continues downwards and also exists at the lowermost depth slice of the model. A similar high-resistivity anomaly is located at the northern boundary of the grid within the northern slope of the elevated pingo. The small low-resistivity anomalies of the second depth slice also continue downwards and become larger with increasing depth. While they are only a few meters in diameter in the second depth slice, they grow up to a few decameters in diameter in the lowermost depth slice of the model. The largest of these low-resistivity anomalies is located in the central and western part of the grid, whereas an additional low-resistivity anomaly is located in the southwestern part. Because these anomalies are characterized by resistivity values much lower than 1,000 Ωm it must be assumed that they correspond to unfrozen areas or at least partially frozen sediment with high contents of unfrozen water within these zones of the pingo.[50,51] The shape of these anomalies is striking. Both narrow towards the surface, resulting in a chimney-like shape of these features. The shape and the low resistivity values suggest that these structures constitute areas of upwelling water, which flows to the surface due to artesian pressure. This might also explain lower resistivity values in the uppermost layer above these vertical structures: the upwelling groundwater leaks to the
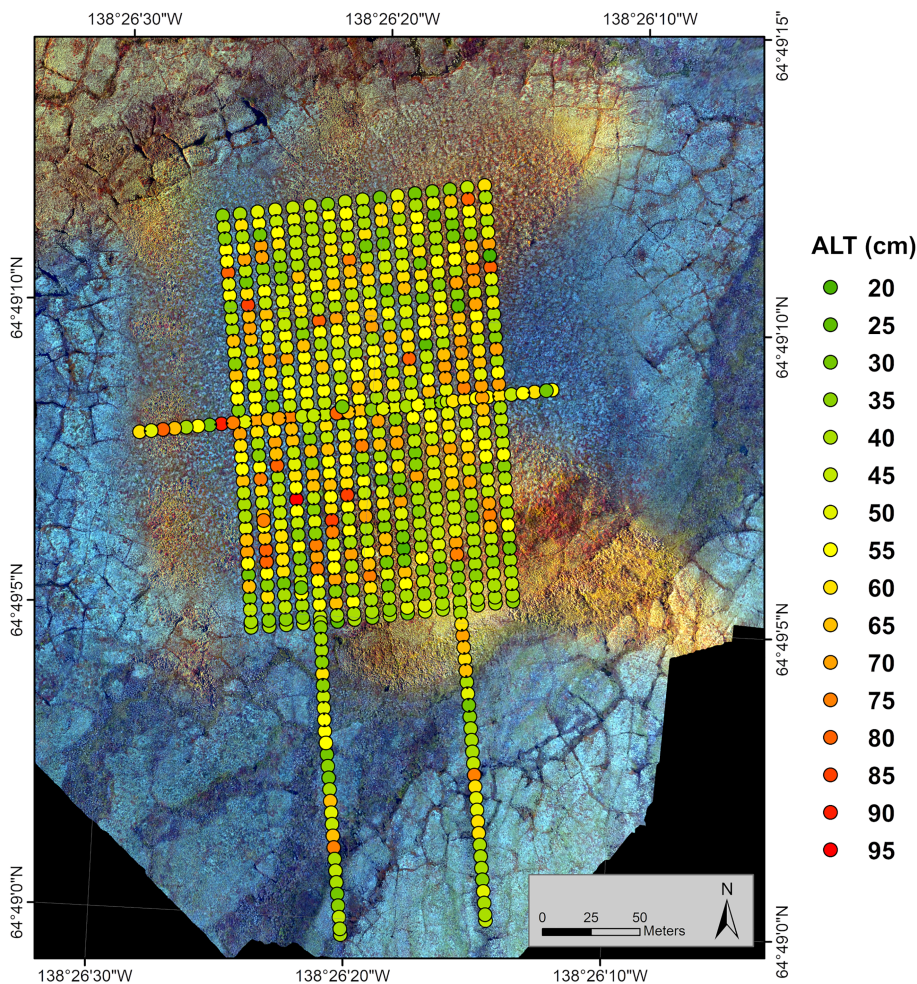
FIGURE 8 Active layer thickness (ALT, cm) at the hydraulic pingo site determined by frost probing. The sampling interval used was set at 6 m (at each second electrode of the quasi-3D grid) [Colour figure can be viewed at wileyonlinelibrary.com]

surrounding area through small springs in the permafrost table, which leads to waterlogging within the active layer of the surrounding area.
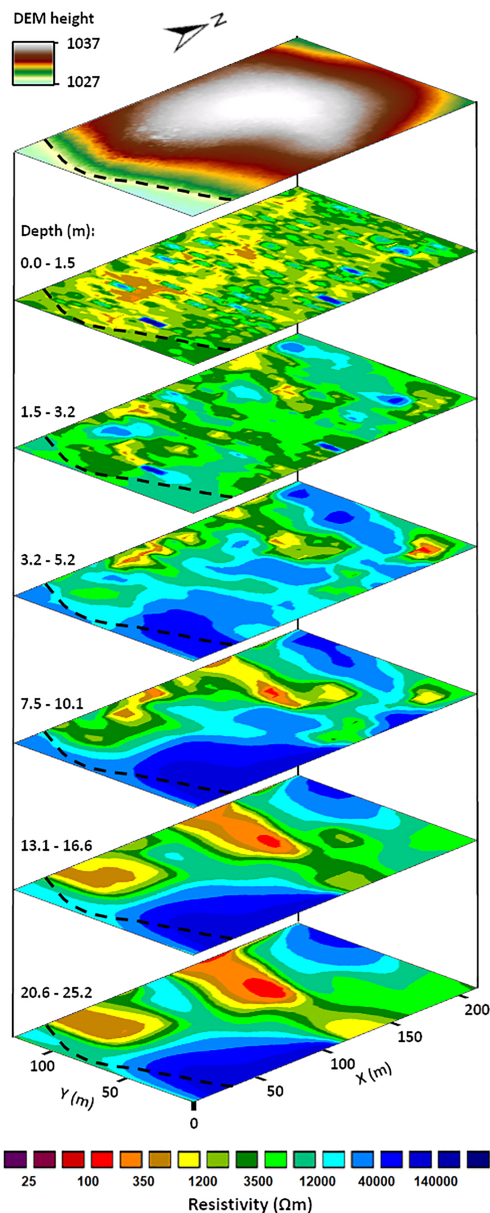
These structures are also visible in the two extended 2D profiles (cf. profile L3 in Figure 10) that include the central part of the pingo as well as the lower end of the hillslope located south of it. The hillslope and predominantly the southern flank of the pingo are underlain by a high-resistivity layer, which is interpreted as ice-rich permafrost due to the high resistivity values. In the central part of the pingo, low-resistivity anomalies are visible. In particular, the narrowing of these anomalies in surface direction and the small interruptions of the surface-parallel permafrost layer are clearly visible in the 2D profiles. Furthermore, the extended profiles show only minimal impact and just slight depth effects of the crossed creeks. It appears that the creeks at this location lead only to minor heat transportation into the underlying permafrost.

5 | DISCUSSION

5.1 | Methodological approach

A quasi-3D approach using ERT to investigate the internal structures of morphological features in periglacial landscapes has rarely been used so far. Nevertheless, the studies in which this approach was used were able to provide high-resolution models of the subsurface, which already showed small-scale variabilities and the heterogeneity of the subsurface.[52–54] In particular, these small-scale variabilities may have a major impact on the investigation of processes and interactions between the surface and subsurface, as shown by the connection of the active layer and the underlying talik at the hydrostatic pingo site. Using an adjusted electrode spacing and interline spacing, this method enables the detection of different features of various scales within the subsurface (e.g.,[52,55]). In this study, the electrode and interline spacings as well as the electrode array were chosen considering site accessibility, power consumption, and the targets of interest. The poor accessibility of the hydraulic pingo site in the Ogilvie Mountains led to greater effort and less effective fieldwork. Therefore, and especially due to limited power supply, a smaller number of measurements but also a smaller number of quadrupoles in each transect could be measured at this site. Use of the dipole–dipole array exploiting the multichannel capabilities of the device would have saved time, but would have resulted in a significantly higher current flow due to the smaller distance between the current electrodes in the partially water-saturated active layer, and thus more battery consumption. At the hydrostatic pingo located very close to the Dempster

FIGURE 9 Quasi-3D ERT results and UAV-based DEM of the hydraulic pingo. Presented are selected depth slices of the quasi-3D ERT grid dataset, which is characterized by an absolute error of 4.41% using the 4th iteration [Colour figure can be viewed at wileyonlinelibrary.com]

parallel to the gridlines were not expected, cross-profiles were unnecessary at this site.[55,56] The detected features mentioned within the results show that the chosen interline spacings are suitable for these sites and also provide datasets of high accuracy and high spatial resolution with low absolute errors (4.73% and 4.41%). This can be due to good ground coupling of the electrodes because of the low resistivity within the moist active layer and also due to the precise arrangement of the grid. In particular, the ground coupling led to good data quality in the 2D profiles, so that less than 1% of the datum points had to be eliminated. Based on the assumption that there are sharp boundaries in the subsurface due to the high contrast between unfrozen areas and ice-rich permafrost, the robust inversion (L1 norm) was used for inversion, which emphasizes such sharp boundaries. Because the surface and the shallow subsurface appeared to be relatively heterogeneous due to varying humidity conditions and soil properties, a relatively low damping factor of 0.1 was used for the surface layer in the inversion model. This provided good representation of the spatial heterogeneity without having a large impact on the model error. As no special spatial orientation of certain objects was to be expected, horizontal and vertical flatness filters were weighted equally.

When comparing the 2D profiles in longitudinal and cross-directions at the hydrostatic pingo site, a slight variation of the resistivity values is visible, especially regarding the high-resistivity anomaly. This is due to so-called "3D-effects", which can occur during 2D resistivity measurements.[55,57] The resulting differences between the measured 2D profiles and the extracted 2D cross-sections of the 3D-inverted grid dataset as mentioned by Emmert & Kneisel[54] could also be observed in our datasets and have to be considered during analysis and interpretation.

A threshold value for the differentiation of frozen and unfrozen conditions could not be determined precisely. However, based on the cross check with frost probing results, it could be assumed that the threshold value should be in the range 800–1,000 Ωm at the hydrostatic pingo site and slightly higher (1,000–1,200 Ωm) at the hydraulic pingo site. These values are quite low, but similar or even lower threshold values were also used in studies in similar permafrost environments.[51,58,59] These materials can contain a high content of liquid water even in the cryotic state ($T < 0°C$)[20,50] resulting in low electrical resistivity values. In addition to the water content, the pore water chemistry can have an influence on the electrical resistivity. In the area of the Mackenzie Delta, for example, high pore water conductivities are expected due to the accumulation of soluble ions as a result of regular flooding, while in elevated regions (i.e., also in the area of the investigated pingos) lower conductivities are more likely to be expected due to eluviation.[60] Hence, the applied threshold values appear realistic, especially because they have also been confirmed by another study in the vicinity of Parsons Lake near the hydrostatic pingo.[61]

The use of GPR to determine the active layer depth in tundra landscapes is already common (e.g., [49,62–64]) but the heterogeneous distribution of soil moisture and different vegetation types make a 3D approach to this method particularly difficult. The time–depth

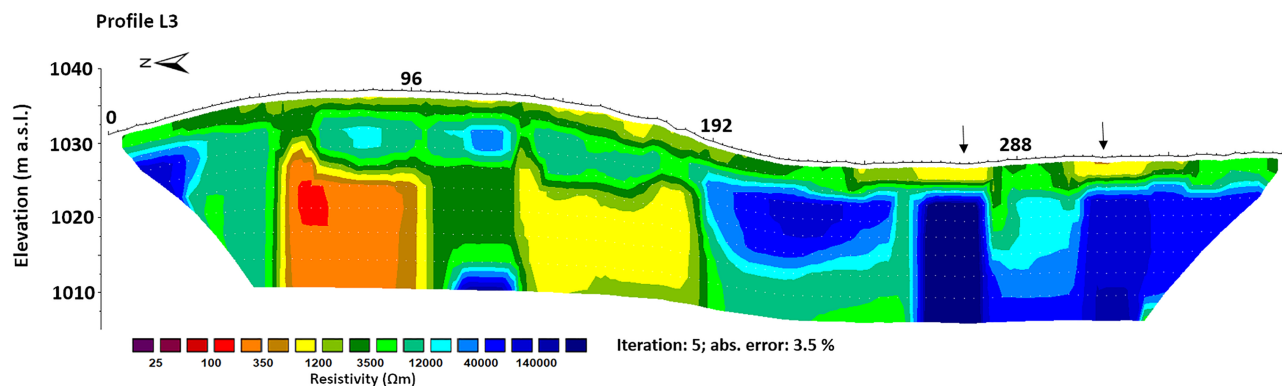Highway these issues were not limiting factors and an additional external power supply could be used.

Another aspect is the scale of interest at each site. Whereas at the hydrostatic pingo site the small-scale variability of the active layer and smaller heterogeneities are of interest, the focus at the hydraulic pingo site was mainly on the detection of unfrozen or aquiferous layers beneath the pingo. Some previous studies using ERT could confirm massive ice cores at hydraulic pingo sites,[19] but often there was no evidence of unfrozen layers beneath. To investigate this, a larger penetration depth is necessary and, consequently, a lower spatial resolution. Because narrow longitudinal structures such as ice wedges

Profile L3

FIGURE 10 ERT profile L3 at the hydraulic pingo site. The regular grid-profile was extended to the south-bordering hillslope using a roll-along approach. The two black arrows mark the positions of two small crossed streams [Colour figure can be viewed at wileyonlinelibrary.com]

conversion is quite complicated because of the small-scale change in soil moisture, which makes data processing and interpretation much more difficult (e.g., [64,65]). Combined with direct frost probing, this removes the problem due to the opportunity of cross-checking the results, but it cannot eliminate all uncertainties and deviations. It must be noted that the active layer depths measured by frost probing lies within an accuracy of 5 cm. The reason for this is the vegetation at the surface, which does not allow a clear delineation of the ground surface, in this case of a thick and compressible moss layer.

The average electromagnetic wave velocity determined within the active layer is 0.057 m/ns. Note that due to the high ice content in the permafrost, the velocity is probably markedly higher than 0.1 m/ns below the permafrost table and the time–depth conversion is therefore only valid for the active layer. Because of the impermeable ice-rich layer next to the permafrost table, the active layer is characterized by relatively high water contents. This water leads to slow propagation velocities and a high signal attenuation within the active layer.[48] An investigation of internal structures within the permafrost body is therefore only possible to a limited extent, except the detection of ice wedges. At first sight the results of frost probing (Figure 4) and GPR-based permafrost table detection (Figure 5) seem to show different structures and the GPR results appear to be more heterogeneous. This is probably mainly an effect of the different sample interval of the two methods. Whereas the sampling interval of the frost probing was 6 m, the virtual sampling interval of the GPR in Figure 5 was set to 1 m. The latter enabled a much more detailed detection of heterogeneities in frost table topography and allowed a visualization of ice-wedge polygons. Although some of these were detected at individual points during frost probing, they do not appear as a coherent network due to the 6-m sampling interval and the resulting low data density. Nevertheless, a certain error also exists due to the heterogeneous humidity conditions in the active layer, which lead to only limited applicability of the GPR calibration based on frost probing results. The determined propagation velocity is an average value, whereas the actual velocities are quite variable within a wide range due to the different moisture contents. A direct comparison of the datasets shows that the ALT determined by GPR tends to be overestimated, especially in the area of the ice wedges, probably

due to the higher moisture content in these depressions. On the other hand, the ALT is underestimated in dryer areas of the grid. Nevertheless, the use of GPR enables good detection especially of relative changes in ALT. In combination with frost probing it delivers comparatively high-resolution information about the ALT and the frost table topography.

5.2 | Internal structure of the hydrostatic pingo

The internal structure of the hydrostatic pingo roughly corresponds to the expected subsurface architecture from previous studies.[2,66] The central part of the pingo is characterized by a massive ice core, whose uppermost boundary is 2–3 m below the ground surface. Its vertical extension cannot be determined because the lowermost edge is deeper than 20 m below the surface and thus below the maximum depth of the pseudosections. In principle, the occurrence of a talik also fits the conceptual model of hydrostatic pingo formation.[2] However, the shape and the location of the detected structures do not fit ideally to the general models.[66] Due to the morphological shape of the pingo, the massive ice core would be expected in a central position below the elevated surface. In contrast, the adjacent talik would be expected to be predominantly below the massive ice core. In this study we found that the shape of the pingo differs significantly from the shape of the underlying massive ice core. While the elevated part of the pingo is characterized by an oval shape, the underlying ice core is more elongated. Moreover, its position is not centered below the elevated surface, but rather beneath the western flank of the pingo. It is striking that the position of the boundary between the massive ice core and the talik and the position of a distinct frost crack at the surface of the pingo are at the same location. At first sight, the steep flank of the ice core seems unusual, but agrees with observations on pingos from other studies (e.g.,[17]). This boundary is located near the center of the pingo and the eastern flank is underlain by a talik or at least partly unfrozen sediments containing large amounts of liquid water.

Consequently, the question arises why the central and western parts are completely frozen and ice-rich, whereas the eastern flank is

underlain by a talik despite probably similar thermal conditions. Based on high-resolution optical satellite data (Planet Scope, Rapid Eye[67]), the effects of varying isolation due to different snow cover thickness or different duration of snow cover can be ruled out, because no asymmetric snow melt is visible in the area of the pingo. Even if the pore water conductivity and the salinity are low, pore water expulsion and solute rejection during refreezing of the former sublake talik could have caused an accumulation of salts in the remaining pore water, which now ensures a significantly lower freezing point of the water.[68] However, because no boreholes were drilled to sample the pore water, this can neither be proven nor falsified. Another possibility is that the eastern part of the drained lake stayed ponded for a longer period, so that the refreezing in this area started later and the talik was isolated for longer time. Such sequenced lake drainages are quite common in this region,[69] but in the investigated drained lake, there is no morphological evidence for this. The remaining pond must have been deeper than two-thirds of the late winter lake ice thickness, which is about 1.5–2 m in this region, to contribute to talik genesis.[69,70] However, because other factors such as advective heat flows through migrating water play a role during refreezing of the talik[70,71] it is not clear whether even a very shallow pond can prevent the talik from refreezing. Nevertheless, this could not be ruled out. At least in modern times it is probable that the thermal conditions are also influenced by advective heat flow from surface water, which drains into the investigated drained lake basin. The water originates from a small lake that is located in a depression south of the investigated drained lake basin (cf. Figure 2b), which is separated by a small terrain step. In high-resolution satellite data from 2017 to 2020 (Planet Scope, Rapid Eye[67]) this thermal impact is visible in late autumn/early winter during refreezing and initial snow cover development. Advective heat flow could also influence the top-down refreezing of the talik.

The current state of a pingo can be deduced, among other things, from the thickness of the layer overlaying the massive ice core. The ratio of the thickness of the overburden material to the base height of the pingo, which is normally between 1:2 and 1:3,[6,66] can also be roughly confirmed. The thickness of the overburden material is around 2.5 m and the relative height of the pingo 4.5 m, so that the ratio is 1:1.8. In combination with the still existing talik or at least liquid water, this ratio indicates that there might be potential for ongoing growth of the pingo. However, the detected linkage between the active layer and the underlying at least partly unfrozen area suggests that there was no isolated talik and thus no hydrostatic pressure at the time of the measurements (end August 2019). It is thus not clear whether the pingo is still growing or whether it has already reached its maximum height. Under these circumstances a closed system is present only during winter and spring, when the active layer is frozen. It is doubtful whether this seasonal hydrostatic pressure is sufficient to enable ongoing uplift of the land surface. However, it is not clear whether the linkage between the active layer and the talik might exist only in years with particularly large ALTs, or whether the linkage might have emerged only in recent years due to increasing ALTs in the context of global warming. Because the (partly) unfrozen sediments are located below the eastern flank of the pingo, the question arises as to how it could have been possible that this part has been uplifted despite the absence of a massive ice core and hydrostatic pressure at least in modern times. In contrast, high ice contents in the area of the western flank could not contribute to strong uplift of the land surface. Instead, based on the theoretical models of hydrostatic pingo formation,[8,66] the water pressure within the closed talik should contribute to water upwelling, resulting in near-surface freezing of the water. The freezing water expands and leads to surface uplift. In this case a massive ice lens should be expected above the talik. The geophysical models show the occurrence and a differing location of the talik or (partly) unfrozen sediments and the ice core, where the unfrozen area is surrounding or at least alongside the ice core. The main differences between the theoretical situation and the results of our investigated hydrostatic pingo are shown in a simplified illustration in Figure 11.

5.3 | Internal structure and water source of the hydraulic pingo

The internal structure of the hydraulic or open-system pingo in the Ogilvie Mountains differs strongly from that of the hydrostatic pingo. Even though the origin of the upwelling water is still unknown, the internal structure of the pingo is similar to the that proposed by Liestøl.[13,14] The ERT data show a large anomaly of low resistivity values in the subsurface of the pingo, which is interpreted as unfrozen
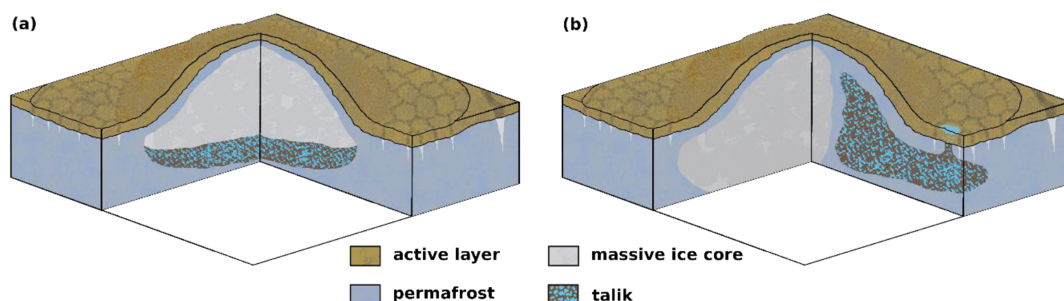
FIGURE 11 Schematic illustration of the differences in the internal structure of a hydrostatic pingo according to theory (a) and the findings based on our ERT model (b) [Colour figure can be viewed at wileyonlinelibrary.com]

and/or water-bearing sediments. This area is of characteristic shape, which tends to narrow in the surface direction. This fits with the observations of Liestøl,[14] who detected some springs of only a few centimeters in diameter near the top of a pingo in Spitzbergen. In particular, the small diameter of the springs in the upper part of the pingo enables high hydraulic pressures and prevents freezing of the upwelling water.[14] The geophysical model provided by the ERT measurements could point to similar processes in our case. The surrounding areas, especially beneath the northern and southern slopes of the pingo, are characterized by high electrical resistivity values, indicating frozen and ice-rich conditions within the subsurface.[50,51] However, a clearly delineated massive ice core as was presented by Yoshikawa et al.[19] could not be detected. Nor is it possible to make a clear differentiation between the pingo ice and the permafrost in the surroundings based on the electrical resistivity values. This might be due to low temperatures and/or ice-rich permafrost in the surrounding area, which is also characterized by high resistivity values. Similar results were presented by Ross et al.,[20] who revealed low resistivity anomalies within two pingos in Svalbard. They argued that the pingos are below the maximum Holocene marine limits and that the low resistivity values result from fine-grained marine sediments (clay) in which the pingos occurred. This can be negated due to the high elevation of the pingo at our investigated site. Because there is no evidence of such fine-grained sediments in the region of the hydraulic pingo in the Blackstone River Valley, the low resistivity values are related to higher water contents also in (slightly) coarser sediments such as glacial till, or fluvial sediments.

The slightly higher ALTs in the area of the potential springs could also indicate a discharge of water, which leads to heat transfer into the active layer and thus to a slightly deeper ALT.[72] The origin of the water is still unknown, but the ERT data indicate that the water flows upwards from a depth of more than 20 m. However, it is also possible that water pathways from a westerly direction towards the pingo occur at shallower depth. This cannot be excluded due to the lack of data coverage, but will be investigated by further measurements at this site during the course of the next year. In the catchment area there are no glaciers or perennial snow patches at present, so that the theory of Liestøl[13] is not an option in this case. Nor are there any known geological faults located in this part of the Blackstone River Valley,[73] so that the theories of O'Brien[12] or Yoshikawa and Harada[15] can be discarded in this case. A potential origin of the artesian groundwater could be the geological interface between two different geological formations in the south-bordering hillslope. Whereas the lower slopes and the valley floor are underlain by Ordovician shales and chert, Devonian slates, arenites and wackestones comprise the uppermost part of the south-bordering hillslope.[73] A layer of coarse-grained scree may also contribute to groundwater flow within the adjacent slope, as suggested by Humlum et al.[16] In this case a connection to the small streams, which originate in the southern hillslope and surround the pingo, would be possible. However, in the immediate vicinity of the pingo there is no connection between the artesian ground water and the small streams, so there can only be a seasonal feed by surface water as discussed by Worsley and Gurney.[23] The ERT data of the two extended profiles show that the streams have only shallow effects on the frost table topography and that there was no connection to the underlying talik. However, possibly further up slope, where the streams are more deeply incised and permafrost may be less ice-rich, there could be a connection between the streams and the talik. Even the presence of major taliks beneath the valley bottom of the broad Blackstone River Valley cannot be ruled out. Groundwater flow beneath and beside the river channel of the Blackstone River has regularly caused large icing events during the winter months only a few kilometers northeast of the pingo near Chapman Lake[39] and also a few kilometers southwest of the pingo in the past.[42] Near Chapman Lake an unfrozen and aquiferous layer was found under partly ice-rich gravels and diamicton till, even away from the actual riverbed.[39] The current altitudinal difference between the surrounding area of the pingo and the actual altitude of the riverbed is about 10 m. However, as confirmed by the analysis of lake sediments of the Chapman Lake, at about 12,500 BP the river bed was 10 m higher at least. At that time the western fork of the Blackstone River passed through the lake. Not until the west fork was captured by the east fork south of the Chapman Lake was the west fork incised to a level lower than the level of Chapman Lake.[41] Hence, connections between a talik beneath the Pingo and taliks of the former Blackstone River West Fork might be present.

6 | CONCLUSION & OUTLOOK

The combined approach using quasi-3D ERT, 3D GPR and frost probing allowed a detailed investigation of a hydrostatic pingo near Parsons Lake (NWT, Canada) and a hydraulic pingo in the Ogilvie Mountains (YT, Canada). In both cases the frost probing enabled comprehensive detection of the permafrost table. At the hydrostatic pingo the ALT shows a significant zonation of lower values in the area of the pingo and higher values in the surrounding area. Also frost cracks detected by GPR influence the ALT at the hydrostatic pingo site. In contrast, the ALT shows no zonation at the hydraulic pingo site. There, more heterogeneous ALTs are noticeable without a significant correlation to relief positions or vegetation patterns.

The results of the ERT measurements presented new insights into the location of massive ground ice and adjacent taliks at both pingo sites. The massive ice core of the hydrostatic pingo is not located below the center of the elevated pingo, as would be expected, but rather within the western flank of the elevated pingo. The eastern flank of the pingo is underlain by a thin, less icy permafrost layer and an underlying layer of probably unfrozen, water-saturated sediments. In contrast to the results of previous pingo-related studies, the remnant of the former talik is located adjacent to the massive ice core of the broad-based pingo within the eastern flank of the pingo and the surrounding low-relief area. Whether there is also a talik below the massive ice core could not be clarified due to the lack of penetration depth beyond the massive ice core. Therefore, the results showed that the internal structures of hydrostatic pingos can be quite different. Consequently, there is a need for further investigations to

understand the formation of massive ice as well as the interactions between massive ice and taliks in the subsurface.

The investigated hydraulic pingo and its internal structures fit with the assumptions and results of some former studies. In the center of the pingo there is a chimney-like feature, which seems to be unfrozen. Hence, it is interpreted as the pathway of unfrozen, upwelling artesian water. However, the origin of this artesian water could not be clarified. It is also notable that there is no massive ice core that could be detected by the ERT measurements. More specifically, the northern and southern flanks of the pingo are underlain by ice-rich permafrost, but there is no clear delineation to the surrounding area. This might be due to high ice contents also in the surrounding area of the pingo.

The combined approach enabled us to derive the first (to our knowledge) 3D geophysical models of hydrostatic and hydraulic pingos. In the case of the hydrostatic pingo, differences to the common theoretical models of internal pingo structures could be deduced. At the hydraulic pingo site, the assumptions of former studies were confirmed in a 3D model. In this case, however, the origin of the artesian water is not fully clear and needs further investigation. Because in both cases (hydraulic and hydrostatic pingos) the migration of water within or beneath the permafrost plays a key role during formation,[66] further knowledge about the ongoing processes is of particular interest, especially in the context of climate change and the associated loss of permafrost and the potential expansion of taliks. Hence, there is a need for further investigations and discussion of pingo formation.

ACKNOWLEDGEMENTS

DATA AVAILABILITY STATEMENT

The data that support the findings of this study are available from the corresponding author upon reasonable request.

ORCID

Julius Kunz https://orcid.org/0000-0003-3689-9575
Christof Kneisel https://orcid.org/0000-0002-5348-9001

REFERENCES

1. French HM. *The Periglacial Environment - 4th Edition*. Chichester, UK: John Wiley & Sons; 2017. https://doi.org/10.1002/9781119 13e2820

2. Mackay JR. Pingos of the Tuktoyaktuk Peninsula Area, Northwest Territories. *Géogra Phy Quate*. 1979;33(1):3-61. https://doi.org/10.7202/1000322ar

3. Richardson J. *Arctic Searching Expedition: Volume 1*. London, UK: Brown, Green & Longmans; 1851.

4. de Leffingwell E K. The Canning River Region, Northern Alaska: U.S. Geological Survey Professional Paper 109; U.S. Geological Survey; 1919.

5. Porsild AE. Earth Mounds in Unglaciated Arctic Northwestern America. *Geogr Rev*. 1938;28(1):46-58. https://doi.org/10.2307/210565

6. Mackay JR. Pingos of the Pleistocene Mackenzie delta area. *Geograp Bull*. 1962;18(2):1-63.

7. Mackay JR. The world of underground ice. *Ann Assoc Ame Geogra*. 1972;62(1):1-22. https://doi.org/10.1111/j.1467-8306.1972.tb00839.x

8. Mackay JR. Pingo Growth and collapse, Tuktoyaktuk Peninsula Area, Western Arctic Coast, Canada: a long-term field study. *Géogra Phys Quater*. 1998;52(3):271-323. https://doi.org/10.7202/004847ar

9. Mackay JR. Growth of Ibyuk Pingo, Western Arctic Coast, Canada, and some implications for environmental reconstructions. *Quatern Res*. 1986;26(1):68-80. https://doi.org/10.1016/0033-5894(86)90084-0

10. Mackay JR. The growth of pingos, Western Arctic Coast, Canada. *Can J Earth Sci*. 1973;10(6):979-1004. https://doi.org/10.1139/e73-086

11. Müller F. Beobachtungen über Pingos: Detailuntersuchungen in Ostgrönland und in der kanadischen Arktis. Copenhagen: CA Reitzels forlag; 1959.

12. O'Brien R. Observations on Pingos and Permafrost Hydrology in Schuchert Dal, NE Greenland. In: Meddelelser om Gronland, 1971; 195(1):1-20.

13. Liestøl O. Pingos, springs and permafrost in Spitsbergen. In: *Norsk Polarinstitutt Arbok 1975*. Norsk Polarinstitutt; 1977:7-29.

14. Liestøl O. Open-system pingos in Spitsbergen. *Norsk Geografisk Tidsskrift - Norweg J Geog*. 1996;50(1):81-84. https://doi.org/10.1080/00291959608552355

15. Yoshikawa K, Harada K. Observations on nearshore pingo growth, Adventdalen, Spitsbergen. *Permafr Periglac Process*. 1995;6(4):361-372. https://doi.org/10.1002/ppp.3430060407

16. Humlum O, Instanes A, Sollid JL. Permafrost in Svalbard: a review of research history, climatic background and engineering challenges. *Polar Res*. 2003;22(2):191-215. https://doi.org/10.1111/j.1751-8369.2003.tb00107.x

17. Demidov N, Wetterich S, Verkulich S, et al. Geochemical signatures of pingo ice and its origin in Grøndalen, west Spitsbergen. *Cryosphere*. 2019;13(11):3155-3169. https://doi.org/10.5194/tc-13-3155-2019

18. Ross N, Harris C, Christiansen HH, Brabham PJ. Ground penetrating radar investigations of open system pingos, Adventdalen, Svalbard. *Norsk Geografisk Tidsskrift - Norw J Geogra*. 2005;59(2):129-138. https://doi.org/10.1080/00291950510020600

19. Yoshikawa K, Leuschen C, Ikeda A, et al. Comparison of geophysical investigations for detection of massive ground ice (pingo ice). *J Geophys Res*. 2006;111(E6):1-10. https://doi.org/10.1029/2005JE002573

20. Ross N, Brabham PJ, Harris C, Christiansen HH. Internal structure of open system pingos, Adventdalen, Svalbard: the use of resistivity tomography to assess ground-ice conditions. *J Environ Engi Geoph*. 2007;12(1):113-126. https://doi.org/10.2113/JEEG12.1.113

21. Hornum MT. *Postglacial Rebound, Permafrost Growth, and Its Impact on Groundwater Flow and Pingo Formation - An Investigation Combining Electrical Resistivity Tomography*. Adventdalen, Svalbard: Hydrogeochemistry and Decoupled Heat and Groundwater Transport Modelling; 2018.

22. Rossi G, Accaino F, Boaga J, Petronio L, Romeo R, Wheeler W. Seismic survey on an open pingo system in Adventdalen Valley,

Spitsbergen, Svalbard. *Near Surf Geophy*. 2018;16(1):89-103. https://doi.org/10.3997/1873-0604.2017037

23. Worsley P, Gurney SS. Geomorphology and hydrogeological significance of the Holocene pingos in the Karup Valley area, Traill Island, northern east Greenland. *J Quar Sci*. 1996;11(3):249-262.

24. Grosse G, Jones BM. Spatial distribution of pingos in northern Asia. *Cryosphere*. 2011;5(1):13-33. https://doi.org/10.5194/tc-5-13-2011

25. Karjalainen O, Luoto M, Aalto J, et al. High potential for loss of permafrost landforms in a changing climate. *Environ Res Lett*. 2020;15(10):1-14. https://doi.org/10.1088/1748-9326/abafd5

26. Brown J, Ferrians OJ, Heginbottom JA, Jr., Melnikov ES. (Eds.). Circum-Arctic map of permafrost and ground-ice conditions. In: *Circum-Pacific Map Series CP-45, scale 1:10,000,000, 1 sheet*. Washington, DC: U.S. Geological Survey in Cooperation with the Circum-Pacific Council for Energy and Mineral Resources; 1977.

27. Nill L, Ullmann T, Kneisel C, Sobiech-Wolf J, Baumhauer R. Assessing spatiotemporal variations of Landsat land surface temperature and multispectral indices in the Arctic Mackenzie Delta Region between 1985 and 2018. *Remote Sens (Basel)*. 2019;11(19):1-26. https://doi.org/10.3390/rs11192329

28. Porter C, Morin P, Howat I, et al. ArcticDEM. Harvard Dataverse, V1, Published online 2018. https://doi.org/10.7910/DVN/OHHUKH. Accessed May 28, 2020.

29. Burn CR, Kokelj SV. The environment and permafrost of the Mackenzie Delta area. *Permafr Periglac Process*. 2009;20(2):83-105. https://doi.org/10.1002/ppp.655

30. NWT Centre for Geomatics. Permafrost Map. Government of Canada, Published online 2014. https://www.geomatics.gov.nt.ca/en/resources

31. Murton JB. Stratigraphy and palaeoenvironments of Richards Island and the eastern Beaufort Continental Shelf during the last glacial-interglacial cycle. *Permafr Periglac Process*. 2009;20(2):107-125. https://doi.org/10.1002/ppp.647

32. Government of Canada. Canadian Climate Normals 1981-2010 Station Data - TUKTOYAKTUK A. Published December 4, 2019. https://climate.weather.gc.ca/climate_normals/results_1981_2010_e.html?searchType=stnName%26txtStationName=tuktoyaktuk%26searchMethod=contains%26txtCentralLatMin=0%26txtCentralLatSec=0%26txtCentralLongMin=0%26txtCentralLongSec=0%26stnID=1700%26dispBack=1 Accessed May 28, 2020.

33. Government of Canada. Canadian Climate Normals 1981-2010 Station Data - INUVIK A. Published December 4, 2019. Accessed May 28, 2020. https://climate.weather.gc.ca/climate_normals/results_1981_2010_e.html?searchType=stnName%26txtStationName=Inuvik%26searchMethod=contains%26txtCentralLatMin=0%26txtCentralLatSec=0%26txtCentralLongMin=0%26txtCentralLongSec=0%26stnID=1669%26dispBack=1

34. Grünberg I, Wilcox EJ, Zwieback S, Marsh P, Boike J. Linking tundra vegetation, snow, soil temperature, and permafrost. *Biogeophysics*. 2020;17(16):4261-4279. https://doi.org/10.5194/bg-2020-88

35. Walker DA, Walker MD, Everett KR, Webber PJ. Pingos of the Prudhoe Bay Region, Alaska. *Arct Alp Res*. 1985;17(3):321-336.

36. Government of Canada. Canadian Climate Normals 1981-2010 Station Data - DAWSON A. Published December 4, 2019. Accessed May 28, 2020. https://climate.weather.gc.ca/climate_normals/results_1981_2010_e.html?searchType=stnName%26txtStationName=Dawson%26searchMethod=contains%26txtCentralLatMin=0%26txtCentralLatSec=0%26txtCentralLongMin=0%26txtCentralLongSec=0%26stnID=1535%26dispBack=0

37. Burn CR. Permafrost, tectonics, and past and future regional climate change, Yukon and adjacent Northwest Territories. *Can J Earth Sci*. 1994;31(1):182-191. https://doi.org/10.1139/e94-015

38. Lacelle D, Lauriol B, Clark ID, Cardyn R, Zdanowicz C. Nature and origin of a Pleistocene-age massive ground-ice body exposed in the Chapman Lake moraine Complex, central Yukon Territory, Canada.

39. *Quatern Res*. 2007;68(2):249-260. https://doi.org/10.1016/j.yqres.2007.05.002

39. Idrees M, Burn CR, Moore JL, Calmels F. Monitoring permafrost conditions along the Dempster Highway. In: *Proceedings, 7th Canadian Permafrost Conference*; 2015.

40. Burn CR, Moore JL, O'Neill HB, et al. Permafrost characterization of the Dempster Highway, Yukon and Northwest Territories. In: *Proceedings, 7th Canadian Permafrost Conference*; 2015.

41. Beierle BD. Late Quaternary glaciation in the Northern Ogilvie Mountains: revised correlations and implications for the stratigraphic record. *Can J Earth Sci*. 2002;39(11):1709-1717. https://doi.org/10.1139/e02-062

42. Crites H, Kokelj SV, Lacelle D. Icings and groundwater conditions in permafrost catchments of northwestern Canada. *Sci Rep*. 2020;10(1):1-11. https://doi.org/10.1038/s41598-020-60322-w

43. Hauck C. *Kneisel C, eds*. Applied Geophysics in Periglacial Environments. Cambridge, UK: Cambridge University Press; 2008. https://doi.org/10.1017/CBO9780511535628

44. Kneisel C, Hauck C, Fortier R, Moorman B. Advances in geophysical methods for permafrost investigations. *Permafr Periglac Process*. 2008;19(2):157-178. https://doi.org/10.1002/ppp.616

45. Reynolds JM. *An Introduction to Applied and Environmental Geophysics*. 2nded. Oxford, UK: Wiley-Blackwell; 2011.

46. Kneisel C, Hauck C. Electrical method. In: Hauck C, Kneisel C, eds. *Applied Geophysics in Periglacial Environments*. Cambridge, UK: Cambridge University Press; 2008:3-27. https://doi.org/10.1017/CBO9780511535628.002

47. Loke MH. Rapid 3-D Resistivity & IP inversion using the least-squares method (For 3-D surveys using the pole-pole, pole-dipole, dipole-dipole, rectangular, Wenner, Wenner-Schlumberger, vector and non-conventional arrays) On land, aquatic, cross-borehole and time-lapse surveys. Malaysia: Geotomosoft; 2019. https://www.geotomosoft.com/r3dimanu.zip Accessed May 20, 2020.

48. Annan AP. Electromagnetic principles of ground penetrating radar. In: Jol HM, ed. *Ground Penetrating Radar Theory and Applications*. Amsterdam, the Netherlands: Elsevier; 2009:1-40. https://doi.org/10.1016/B978-0-444-53348-7.00001-6

49. Moorman BJ, Robinson SD, Burgess MM. Imaging periglacial conditions with ground-penetrating radar. *Permafr Periglac Process*. 2003;14(4):319-329. https://doi.org/10.1002/ppp.463

50. Fortier R, Allard M, Seguin M-K. Effect of physical properties of frozen ground on electrical resistivity logging. *Cold Reg Sci Technol*. 1994;22(4):361-384. https://doi.org/10.1016/0165-232X(94)90021-3

51. Fortier R, LeBlanc A-M, Allard M, Buteau S, Calmels F. Internal structure and conditions of permafrost mounds at Umiujaq in Nunavik, Canada, inferred from field investigation and electrical resistivity tomography. *Can J Earth Sci*. 2008;45(3):367-387. https://doi.org/10.1139/E08-004

52. Rödder T, Kneisel C. Permafrost mapping using quasi-3D resistivity imaging, Murtèl, Swiss Alps. *Near Surf Geophy*. 2012;10(2):117-127. https://doi.org/10.3997/1873-0604.2011029

53. Kneisel C, Emmert A, Kästl J. Application of 3D electrical resistivity imaging for mapping frozen ground conditions exemplified by three case studies. *Geomorphology*. 2014;210:71-82. https://doi.org/10.1016/j.geomorph.2013.12.022

54. Emmert A, Kneisel C. Internal structure of two alpine rock glaciers investigated by quasi-3-D electrical resistivity imaging. *Cryosphere*. 2017;11(2):841-855. https://doi.org/10.5194/tc-11-841-2017

55. Chambers J, Ogilvy R, Kuras O, Cripps J, Meldrum P. 3D electrical imaging of known targets at a controlled environmental test site. *Environ Geol*. 2002;41(6):690-704. https://doi.org/10.1007/s00254-001-0452-4

56. Loke MH, Chambers JE, Rucker DF, Kuras O, Wilkinson PB. Recent developments in the direct-current geoelectrical imaging method.

J App Geophy. 2013;95:135-156. https://doi.org/10.1016/j.jappgeo.2013.02.017

57. Sjödahl P, Dahlin T, Zhou B. 2.5D resistivity modeling of embankment dams to assess influence from geometry and material properties. *Geophysics*. 2006;71(3):G107-G114. https://doi.org/10.1190/1.2198217

58. Lewkowicz AG, Etzelmüller B, Smith SL. Characteristics of discontinuous permafrost based on ground temperature measurements and electrical resistivity tomography, southern Yukon, Canada. *Permafr Periglac Process*. 2011;22(4):320-342. https://doi.org/10.1002/ppp.703

59. Dobiński W. Geophysical characteristics of permafrost in the Abisko area, northern Sweden. *Pol Pol Res*. 2010;31(2):141-158. https://doi.org/10.4202/ppres.2010.08

60. Kokelj SV, Burn CR. Geochemistry of the active layer and near-surface permafrost, Mackenzie delta region, Northwest Territories, Canada. *Can J Earth Sci*. 2005;42(1):37-48. https://doi.org/10.1139/e04-089

61. Angelopoulos MC, Pollard WH, Couture NJ. The application of CCR and GPR to characterize ground ice conditions at Parsons Lake, Northwest Territories. *Cold Reg Sci Technol*. 2013;85:22-33. https://doi.org/10.1016/j.coldregions.2012.07.005

62. Hinkel KM, Doolittle JA, Bockheim JG, et al. Detection of subsurface permafrost features with ground-penetrating radar, Barrow, Alaska. *Permafr Periglac Process*. 2001;12(2):179-190. https://doi.org/10.1002/ppp.369

63. Munroe JS, Doolittle JA, Kanevskiy MZ, et al. Application of ground-penetrating radar imagery for three-dimensional visualisation of near-surface structures in ice-rich permafrost, Barrow, Alaska. *Permafr Periglac Process*. 2007;18(4):309-321. https://doi.org/10.1002/ppp.594

64. Brosten TR, Bradford JH, McNamara JP, et al. Estimating 3D variation in active-layer thickness beneath arctic streams using ground-penetrating radar. *J Hydrol*. 2009;373(3–4):479-486. https://doi.org/10.1016/j.jhydrol.2009.05.011

65. Schennen S, Tronicke J, Wetterich S, Allroggen N, Schwamborn G, Schirrmeister L. 3D ground-penetrating radar imaging of ice complex deposits in northern East Siberia. *Geophysics*. 2016;81(1):WA195-WA202. https://doi.org/10.1190/geo2015-0129.1

66. Gurney SD. Aspects of the genesis and geomorphology of pingos: perennial permafrost mounds. *Progr Phys Geogr: Earth Environment*. 1998;22(3):307-324. https://doi.org/10.1177/030913339802200301

67. Planet Team. Planet Application Program Interface: In Space for Life on Earth.; 2018. https://api.planet.com

68. Mackay JR. A full-scale field experiment (19781995) on the growth of permafrost by means of lake drainage, western Arctic coast: a discussion of the method and some results. *Can J Earth Sci*. 1997;34(1):17-33. https://doi.org/10.1139/e17-002

69. Mackay JR, Burn CR. The first 20 years (1978–1979 to 1998–1999) of ice-wedge growth at the Illisarvik experimental drained lake site, western Arctic coast, Canada. *Can J Earth Sci*. 2002;39(1):95-111. https://doi.org/10.1139/e01-048

70. O'Neill HB, Roy-Leveillee P, Lebedeva L, Ling F. Recent advances (2010–2019) in the study of taliks. *Permafr Periglac Process*. 2020;31(3):346-357. https://doi.org/10.1002/ppp.2050

71. Ling F, Zhang T. Modeling study of talik freeze-up and permafrost response under drained thaw lakes on the Alaskan Arctic Coastal Plain. *J Geophys Res*. 2004;109(D01111):1-9. https://doi.org/10.1029/2003JD003886

72. Shiklomanov NI, Streletskiy DA, Nelson FE, et al. Decadal variations of active-layer thickness in moisture-controlled landscapes, Barrow, Alaska. *J Geophys Res*. 2010;115:1-14. https://doi.org/10.1029/2009JG001248

73. Yukon Geological Survey. Yukon Digital Bedrock Geology. Published 2015. Accessed June 15, 2020. https://www.arcgis.com/home/webmap/viewer.html?webmap=c1544758b4ff4d24ab6638e32b846514